$WTa_{37}O_{95.487}$ Nanocatalyst for Pollutants Degradation

Siti Nur Farhana Mohd Nasir,*[§, †] Habib Ullah,*[‡] Muhazri Abd Mutalib,[†] Farah Husna Saifuddin,[†] Nurul Affiqah Arzaee,[†] Asif Ali Tahir,[‡] Mohamad Firdaus Mohamad Noh,[†] Mohd Adib Ibrahim,[†] Hazim Moria,[¶] Mohammed N. Alghamdi,[¶] Mohd Asri Mat Teridi*[†]

[†]Solar Energy Research Institute (SERI), National University of Malaysia, 43600 Bangi, Selangor, Malaysia.

[§]Department of Community Health, Faculty of Medicine, Universiti Kebangsaan Malaysia, 56000 Cheras, Kuala Lumpur, Malaysia.

[‡]Environment and Sustainability Institute (ESI), University of Exeter, Penryn Campus, Penryn, Cornwall TR10 9FE, UK.

[¶]Department of Mechanical Engineering Technology, Yanbu Industrial College, PO Box 30436, 41912 Yanbu Alsinaiyah, Saudi Arabia.

[*]Email: farhanaana98@gmail.com; hu203@exeter.ac.uk; asri@ukm.edu.my/+603-8911 8580

Abstract

The release of toxic industrial effluents has created serious impacts on human health and the aquatic ecosystem. $WTa_{37}O_{95.487}$ is a wide bandgap material that was reported in 1971 but no one has investigated its photocatalytic properties due to its wide bandgap and unique crystal structure. Herein, we carried out detailed experimental and density functional theory (DFT) simulations of $WTa_{37}O_{95.487}$ nanocatalyst. The influence of temperature and light intensity on their crystallography, morphology, optical, and photocatalytic properties were studied. The powder obtained at 150 °C (WT-1) exhibited higher photocatalytic activity of 99 % of methylene blue dye degradation within 30 minutes with pseudo-first-order kinetics constant of 0.0643 min^{-1}. DFT simulations revealed a good correlation between theory and experiment of electronic properties of $WTa_{37}O_{95.487}$, which consequently validate the catalytic performance of the catalyst. The $WTa_{37}O_{95.487}$ nanocatalyst is proposed as a novel and effective photocatalyst for treating dye effluents of wastewater.

1. Introduction

In recent years, the widespread presence of organic contaminants such as dyes in industrial wastewater has posed a serious threat to human health and the aqueous ecosystem. Textile wastewater is one of the major industrial activities that contribute to environmental pollution because they discharge undesirable dye effluents. The dyes used in the textile industry such as methylene blue (MB) have a heterocyclic aromatic compound that is highly dangerous, carcinogenic even at low concentrations, and cannot be degraded easily by ordinary treatments.[1,2] Therefore, the removal of dyes from industrial effluents before releasing them into the environment is extremely imperative. In recent years, heterogeneous photocatalyst was regarded as a propitious way for the purification of contaminated waters.[3–9] In this perspective, wide bandgap semiconductor photocatalysts have shown their potential capacity in the photocatalytic degradation of environmental pollutants. Tantalum pentoxide, Ta_2O_5 is a promising and efficient photocatalyst that is nearly comparable to the popular TiO_2 photocatalyst owing to its wide bandgap (3.9 eV)[10] and stable solid oxide semiconductor. Ta_2O_5 possesses good chemical and thermal stability and has a high photocatalytic performance to break down organic pollutants in the UV regime.[11] Nevertheless, the wide bandgap of Ta_2O_5 severely limits the absorb photons to create electron-hole pairs. Therefore, in an attempt to improve the charge separation efficiency, Ta_2O_5 was modified by incorporation of W that leads to the shift of some bands in Ta_2O_5 to reduce its bandgap for an effective photocatalytic reaction. Other than band gap tuning, it is well known that the specific characteristic such as morphology is strongly affected by the photocatalytic performance. Porous micro/nanostructure can greatly improve the photocatalytic activity due to the more accessible active site and short diffusion length of charge carriers.[12–14] In this work, the incorporation of W into Ta_2O_5 was synthesized by simple co-precipitation method and the influence of synthesis temperature of tungsten tantalum oxide, $WTa_{37}O_{95.87}$ on the structural, morphology, optical characteristics towards the photodegradation of methylene blue under UV light were investigated. Also, the influence of light intensity on the photodegradation rate of MB was studied by irradiating the $WTa_{37}O_{95.487}$ nanocatalyst with varying irradiation intensities (100 and 200 $mWcm^{-2}$). A possible mechanism of the photocatalytic reaction over $WTa_{37}O_{95.487}$ is proposed. Our results would certainly have a significant impact on the further use of $WTa_{37}O_{95.487}$ as a potential photocatalyst for environmental remediation. In addition, density functional theory (DFT) simulations are performed to countercheck our experimental data. For the first time, we model the structure of $WTa_{37}O_{95.487}$, although, it has been reported by Stephenson et al. in 1971.[15–17] The electronic properties of $WTa_{37}O_{95.487}$ such as band structure, density of states (DOS), partial DOS (PDOS), optical absorption spectra, electron difference density, and Fermi energy are simulated and compared with the experimental data. From the combined theoretical and experimental data, a good correlation is found which consequently validate and confirmed the catalytic performance of the proposed catalyst.

2. Materials and Method

2.1. Synthesis of $WTa_{37}O_{95.487}$ Powder

The catalyst powder was prepared by a facile co-precipitation method as follows: 3 g of EDTA was added into a 150 ml NH_3 solution. 2:1 of Ta_2O_5 and $(NH_4)_6H_2W_{12}O_4 \cdot xH_2O)$ were added into the above solution. The mixture was further stirred and heated at 80 °C for 4 hours and then was dried in the microwave oven at 150 °C for 6 hours and at 200 °C for 4 hours. The samples that were dried at 150 and 200 °C were denoted as WT-1 and WT-2, respectively. The phase and crystallinity of the obtained powder were examined using Powder X-ray Diffractometer (XRD) from Bruker/D8 Advance using Cu-X-ray in the 2θ range from 20° to 80°. The morphology and elemental mapping of the powder were obtained via field emission scanning electron microscopy (FESEM) coupled with energy-dispersive X-ray spectroscopy

(EDX; FE-SEM SUPRA VP55). Optical characterizations were performed by the UV-vis absorption spectrophotometer (PerkinElmer Lambda 950). The photocatalytic activities of WT-1 and WT-2 have been evaluated by the degradation of methylene blue (MB) as the target pollutant and the experiment was conducted at room temperature using a 150 W xenon lamp as a light source. Prior to irradiation, the suspension of the catalyst powders prepared at 150 °C and 200 °C were kept in the dark for 30 minutes to attain adsorption/desorption equilibrium between the dye molecules and catalyst surface with continuous stirring. 0.05 g of the WT-1 and WT-2 was dispersed in 60 ml of MB (10 mg/L) during the reaction. 6 ml of the suspension was filtered through 0.45μm Millipore discs to remove the catalyst agglomerates in suspension from the dye solution at various time intervals of the irradiation period. The photocatalytic degradation rate of methylene blue was expressed according to the following formula (equation 1):[18]

$$\textit{Degradation rate}\ (\%) = \frac{C_0 - C_t}{C_0} \text{ x } 100\% \quad (1)$$

Where C_0 is the initial concentration of methylene blue solution, C_t is the concentration at reaction time, t determine at $\lambda_{max} = 664$ nm. The kinetic of MB degradation against irradiation time can be assumed as the pseudo-first-order kinetics model shown in equation (2):[19]

$$ln\left(\frac{C_0}{C_t}\right) = k_{app}t \quad (2)$$

Where k_{app} is the apparent pseudo-first-order rate constant, C_0 represents the initial concentration of methylene blue at $t = 0$, and C_t represents the instantaneous concentration of MB remaining at different photo-irradiation periods t. The Brunau–Emmet–Teller (BET) N_2 adsorption/desorption isotherm of the as prepared nanocatalysts have been carried with the help of Micromeritics ASAP 2020 M system at a temperature of liquid nitrogen. The ST-2000 constant volume adsorption apparatus was used for the evaluation of BET surface area. The quantum yield, Φ, turnover number (TON) and turnover frequency (TOF) for the photocatalytic decomposition of methylene blue have been calculated by using equation (3, 4 and 5):[20,21]

$$\Phi = \frac{\text{Number of contaminant molecules degraded}}{\text{Number of photons absorbed}} \quad (3)$$

$$\text{TON} = \frac{\text{Number of moles of contaminant degraded}}{\text{Number of moles of catalyst}} \quad (4)$$

$$\text{TOF}=\frac{\text{TON}}{\text{time}} \quad (5)$$

2.2. Computational Methodology

Solid-state density functional theory (DFT) simulations are performed on Quantum-ATK[22] and the results are analyzed on VNL Version 2019.12.[22] In order to represent the experimentally observed $WTa_{37}O_{95.487}$, first, we used the unit cell of Ta_2O_5,[23] having a space group of Pmmm and lattice parameters of, a = 3.88 Å, b = 3.93 Å and c = 13.05 Å, and α, β, γ = 90; taken from the literature.[23] The unit cell has four Ta and ten oxygen atoms hence, cannot be used for the minimum W doping. The perfect model of $WTa_{37}O_{95.487}$ can be built from the 4x4x2 supercell of Ta_2O_5, where two Ta should be replaced with W, followed by the addition of an O atom (see Figure S1b). As we know, $WTa_{37}O_{95.487}$ is a combination of 18.5 Ta_2O_5 and one WO_3, as shown in equation (6) below.[15–17]

$$18.5Ta_2O_5 + WO_3 \rightarrow WTa_{37}O_{95.487} \quad (6)$$

In this case, the ratio between Ta and W is 37:1, hence, in order to build a reliable model of $WTa_{37}O_{95.487}$, at least a 4x4x2 supercell of Ta_2O_5 is required (Fig S1). The unit and supercells of Ta_2O_5 have been optimized at Generalized Gradient Approximation (GGA) with the Perdew-Burke-Ernzerhof (PBE) method, exchange-correlation functional, and pseudopotential of Hartwigsen Goedecker-Hutter (HGH) with tier 4 basis.[24] While the electronic properties such as band structure, optical absorption spectra, the density of states (DOS) and partial DOS

(PDOS), effective potential, electron difference density (EDD), and electron localization functional (ELF) are simulated at GGA/PBE at PseudoDojo pseudopotential.[22,25] The linear combination of atomic orbitals (LCAO) method is used for Ta, W, O, and H atoms.[26] The optimized lattice parameters of bulk Ta_2O_5 have a nice correlation with the previous reports.[15,16,27] Besides, we have also considered the 2x2x2 supercell of Ta_2O_5 for $WTa_{37}O_{95.487}$ and investigated the catalytic activity. The 2x2x2 supercell of Ta_2O_5 has 80 oxygen and 32 Ta atoms. We replaced one of the Ta atoms in a 2x2x2 supercell of Ta_2O_5 with W and constructed minimum possible model of $WTa_{37}O_{95.487}$ nanocatalyst as shown in Figure S2. Asymmetric [001] slabs of Ta_2O_5 and $WTa_{37}O_{95.487}$ are constructed and optimized according to the above mentioned method.[23] A 7x7x7 Monkhorst-Pack k-grid with an energy cut-off of 1500 eV is used for the unit cell, while a 5x5x1 k-point mesh is used for the slabs. In order to check and compare the catalytic activity of $WTa_{37}O_{95.487}$ with pristine Ta_2O_5; we attach one hydroxyl group (OH) on their surfaces and simulate the adsorption energy.

3. Results and Discussion

3.1. Structural Analysis

X-ray diffraction spectra of the prepared photocatalysts are shown in Figure 1a. All the characteristic diffraction peaks at 2θ = 22.90°, 28.30°, 28.95°, 37.14°, 46.79°, 55.59° can be assigned to (0 0 1), (1 19 0), (2 2 0), (2 18 0), (0 0 2), (0 38 0) and (1 19 2) of the orthorhombic tungsten tantalum oxide, $WTa_{37}O_{95.487}$ (JCPDS 01-070-2464, a = 6.188 Å, b = 69.570 Å, c = 3.880 Å). The strong intensity of diffraction peaks indicates better crystallinity for the catalyst powder. Furthermore, no other peaks were detected in the spectra implying the high purity of both samples. The crystallites size of WT-1 and WT-2 calculated based on the peak at (0 0 1), were increased from 55 to 71 nm respectively indicating that larger crystallite size attributed to the thermally promoted crystalline growth in high temperature. As the synthesis temperature rise, the crystal grain begins to grow and re-organize to form a crystal cluster.[28] Since the growth orientation of the crystal grain depends on the energy absorbs from the heat due to the increase in temperature hence, the orientation of crystal growth exploits the vacancy position between the crystal cluster[29] and consequently increases the crystallite size.[30] Figure 1 (b, c) portrays the surface morphology of the WT-1 and WT-2. The morphology of WT-1 (Figure 1b) is comprised of porous granular shapes. It can be seen that the aggregation creates substantial pores and rough surfaces that are suitable for dye trapping and adsorption. Thus, WT-1 has a larger accessible active site for photocatalytic reaction. On contrary, the FESEM image of WT-2 (Figure 1c) showed different morphology where the particles are merged causing dense agglomeration. Both WT-1 and WT-2 have an average particle size of about 310 and 210 nm, respectively (Figure S3). The elemental presence of the constituents in the nanocatalyst is confirmed through EDX and elemental mapping as presented in Figure 1 (d, e, f). The EDX spectrum shows high peaks of Ta and W followed by O and detected no other impurities which indicate the nanocatalyst are well-crystallized which are in accordance with the XRD results. The images from elemental mapping undoubtedly proved that powder nanocatalyst contains W, Ta, and O elements. However, as seen in Figure 1f, small amounts of W and Ta were detected on the catalyst surface of WT-2. Therefore, fewer free radicals are generated for the photocatalytic reaction. Since, catalysis belongs to the class of surface reaction, thus, huge specific surface area could remarkably promote the photocatalytic performance of the photocatalyst. In order to confirm whether the surface area contribute to the enhanced activity of the as-fabricated WT-1 nanocatalyst, we measured BET nitrogen adsorption-desorption isotherm curves of both WT-1 and WT-2 as provided in Figure S4. It is obvious that WT-1 exhibited large specific surface area i.e. 62.1 m^2g^{-1} compared to that of WT-2 (45.7 m^2g^{-1}). Thus, we can say the enhanced photoactivity is related to the corresponding large surface area.

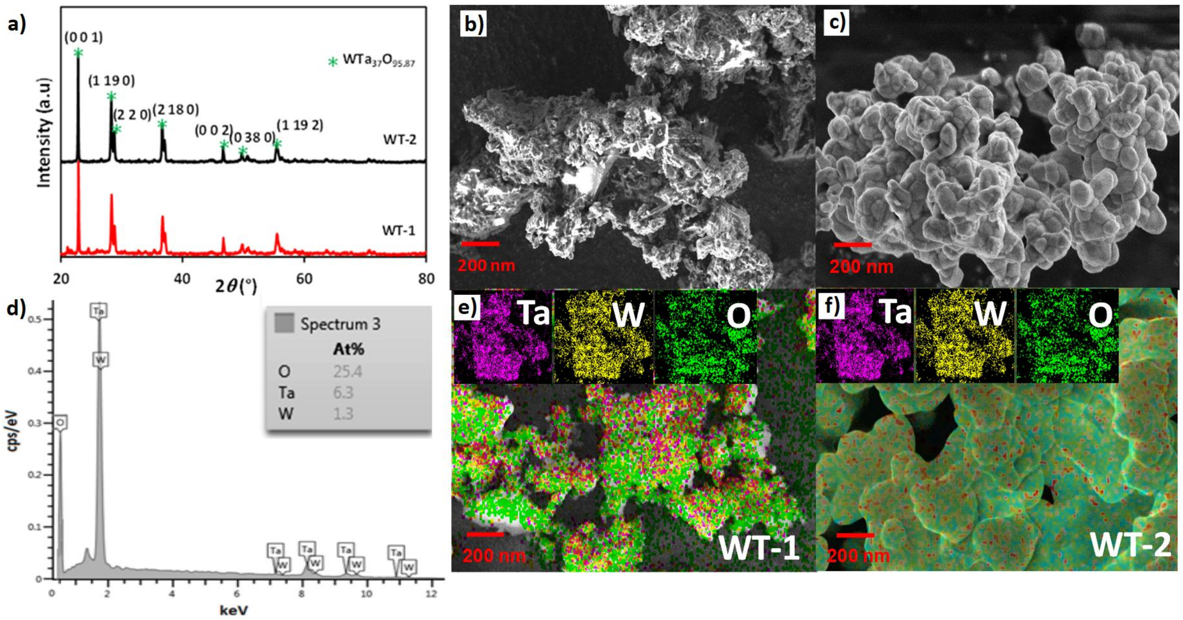

Figure 1. (a) XRD pattern and (b, c) surface morphology of WT-1 and WT-2. (d) The EDX spectrum and (e, f) elemental mapping of WT-1 and WT-2.

3.2. Optical Properties

To evaluate the optical properties of the obtained catalyst, the absorption spectra of the WT-1 and WT-2 are illustrated in Figure 2a. The major absorption band of both samples that appear near 300 nm is evidence that the photocatalytic activity of WT-1 and WT-2 are driven predominantly by UV light. The WT-2 exhibits a low absorption spectrum than WT-1 and blue shift at 300 nm signifying an increase in the bandgap values. The bandgap energy of the synthesized catalyst can be estimated by extrapolating the graph from the Tauc plot in Figure 2b. The estimated bandgap of WT-1 and WT-2 is 3.73 and 3.92 eV, respectively. This wide-bandgap value is in accordance with the UV characteristics of the $WTa_{37}O_{95.487.}$ The slightly shifted absorption edge from a longer wavelength to a shorter wavelength implies that the temperature can play a vital role in changing the absorption characteristic of the catalyst.

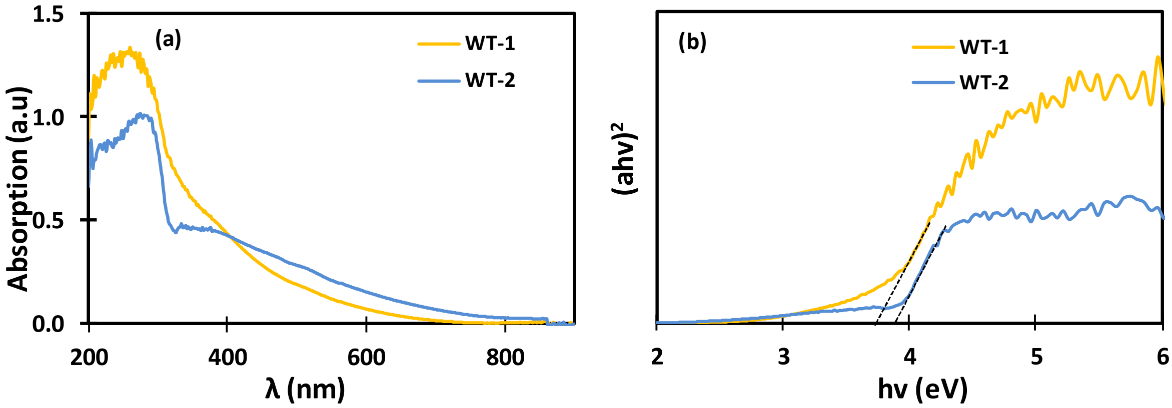

Figure 2. (a) UV-visible absorption spectra and (b) Tauc plots of WT-1 and WT-2.

3.3. Photocatalytic Properties

The photocatalytic degradation of MB under UV light is depicted in Figure 3. The catalytic degradation of the MB dyes in the presence of 0.05 g catalyst was observed visually by the change in color. The intensity of the color gradually decreased with time after adsorption/desorption equilibration (t_0) for WT-1. The decoloring of methylene blue after 30 minutes of adsorption/desorption attributed to the oxidative attack on the central ring of MB with resulting loss of electronic delocalization due to the solvatochromism effect.[31] For WT-1, after 30 minutes of irradiation (t_{30}), the color of MB turns to light blue under 100 mWcm^{-2} (inset Figure 3a) and it achieved an almost complete decolorization of the blue color under 200 mWcm^{-2} (inset Figure 3c) marking an effective catalytic degradation activity of WT-1 in the presence of sunlight. Meanwhile, the decolorization of dye for sample WT-2 was observed after 240 min of irradiation as seen in inset Figure 3 (b, c). Thereafter, the degradation of MB was analyzed spectroscopically by obtaining an absorption band of the dye solution as shown in Figure 3. Initially, the as-prepared MB dye displayed a maximum absorption in 640 – 650 nm owing to the n-π* transition of the MB.[32,33] For sample WT-1, the gradual hypsochromic shift of the absorption band from 664 to 614 nm suggested the concurrent N-demethylation of the dimethylamino group of MB. While the slightly hypsochromic shift at 292 nm indicates that the phenothiazine species has been completely decomposed and no other phenothiazine-like intermediates were produced[34] (Figure S5). In this regard, the remarkable catalytic activity of WT-1 is attributed to its porous structure, which favors the adsorption of dye molecules. As seen in Figure 1b, the visible tiny pores embedded in WT-1 acts as a channel for the effective diffusion of methylene blue and facilitates the photoreaction. Moreover, the smaller bandgap of WT-1 accelerates the charge carrier movement upon irradiation and results in the enhancement of degradation rate. In contrast, the efficiency of photo-decolorization slowly decreased for WT-2 because the particle agglomeration in WT-2 makes the powder catalyst less dispersed in the methylene blue solution, which in turn lowers the reactant adsorption. Low dispersibility prevents catalyst suspension from harvesting more light and inadequate exposure to the reactant, hence reduces the photogeneration charge carriers. Owing to the low absorption intensity absorbed by WT-2 (Figure 2a), and small amounts of W and Ta detected on WT-2 (Figure 1f), fewer charge carriers were generated. Furthermore, the charge recombination rate of WT-2 surpasses the rate of charge separation in WT-2 due to its large bandgap and particle agglomeration which retards the photocatalytic activity. Approximately 99 % of MB are photo-catalytically degraded by WT-1 after 60 minutes and 30 minutes under 100 and 200 mWcm^{-2}, respectively. Meanwhile, it took 240 min for WT-2 to degrade 74 % and 81 % of MB under the same irradiation. Figure 3 (e, f, g, h) shows the rate of photocatalytic degradation of MB as a function of time C/C_0 at a maximum absorbance λ_{max} = 664 nm. The significant enhanced photocatalytic activity was observed under 200 mWcm^{-2} compared to 100 mWcm^{-2} for WT-1 which inferring the photodegradation rate of MB becomes dependent on light intensity. As shown in inset of Figure 3 (e, f, g, h), the kinetic disappearance of MB was obtained from the plot of $ln\ (C/C_0)$ against illumination time. The apparent time constant, k_{app} for WT-1 was 0.0321 and 0.0643 min^{-1} under 100 and 200 mWcm^{-2}, respectively. Concurrently, k_{app} for WT-

2 is approximately 13 and 20 times smaller than its counterpart. To further assess the photocatalytic efficiency, the quantum yield (Φ), turnover number (TON), and turnover frequency (TOF) were estimated for WT-1 and WT-2. The use of Φ, TON, and TOF concepts as quantitative indicators of catalytic efficiency has been extensively described in batch photocatalytic reaction studies. [21,35,36] These terms are useful to describe the catalyst efficiency in relative terms.[36] Values of Φ, TON and TOF calculated after 60 min are shown in Table 1 and detailed calculations are given in the Supporting Information. In both cases, the higher irradiation intensity (200 mWcm^{-2}) produced a greater TON and TOF value than the lower intensity counterpart (100 mWcm^{-2}). These higher values should be expected, as more photons are available for the catalyst sites and more chemical reactions occurred per hour. Meanwhile, the value of Φ is smaller under higher light intensity because the number of absorbed photons exceed the number of catalyst particles. As a result, only a few number of photons are necessary to excite the catalyst particles and the rest are reflected or absorbed as a heat.

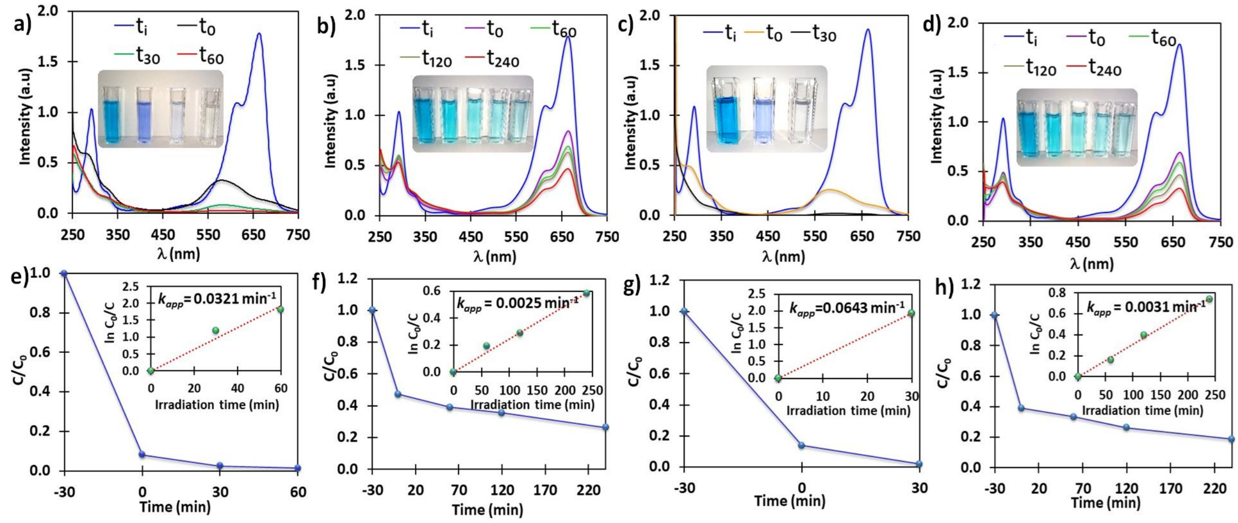

Figure 3. The photocatalytic degradation of methylene blue over (a) WT-1 and (b) WT-2 under 100 mWcm^{-2} irradiation. The photocatalytic degradation of methylene blue over (c) WT-1 and (d) WT-2 under 200 mWcm^{-2} irradiation. The C/C$_0$ vs. the irradiation time under 100 mWcm^{-}

^{2} of (e) WT-1 and (f) WT-2. The C/C_0 vs. the irradiation time under 200 mWcm^{-2} of (g) WT-1 and (h) WT-2. The inset shows the respective kinetics degradation of MB.

Table 1. The C/C_0 and degradation efficiency of methylene blue under different light intensities.

Sample	WT-1		WT-2	
Light intensity (mWcm^{-2})	100	200	100	200
Degradation efficiency (%)	99*	99**	74***	81***
C/C_0 (min^{-1})	0.0321	0.0643	0.0025	0.0031
Quantum yield, Φ	1.09×10^{-3}	5.54×10^{-4}	7.13×10^{-4}	3.90×10^{-4}
Turnover number, TON	8.69×10^{-3}	8.83×10^{-3}	5.40×10^{-3}	5.82×10^{-3}
Turnover frequency, TOF (min^{-1})	1.45×10^{-4}	1.47×10^{-4}	9.00×10^{-5}	9.70×10^{-5}

Note: * Within 60 min of irradiation; ** Within 30 min of irradiation; *** Within 240 min of irradiation

As the light intensity increase, the number of photons striking on per unit area also increases. The separation rate of photoelectrons and holes precedes their recombination rate and thus facilitates the generation of reactive $OH^{\bullet}$ radicals. The generation of electron-hole becomes the uppermost process, resulting in a fast photodegradation rate. Meanwhile, the rate of degradation was sluggish under lower light intensity because electron-hole separation competes with their recombination due to the less formation of free radicals.[37,38] There are more photons per unit time at a higher intensity. Thus, increasing the light intensity has led to a decrease in the time required for dye decolorization. The mechanism that constitutes the photocatalytic degradation of MB is illustrated in Figure 4 and equation (7-12). When the photocatalyst absorbs light, electron-hole pairs are created. The energy from the photon induces the separation of electron-hole pairs. The electron from the valence band moves across the bandgap of the photocatalyst to the conduction band leaving behind a hole. Once the electron reaches the conduction band, it picks up the O_2 acceptor at the catalyst interface to produce superoxide radical anion $O_2^{\bullet}$ that endorses the conversion of H_2O molecule into H_2O_2 and then $OH^{\bullet}$. Meanwhile, the hole at the valence band scavenges by H_2O or hydroxyl group OH^{-} to produce hydroxyl radical $OH^{\bullet}$. The existence of reactive $OH^{\bullet}$ radical is a dominant oxidizing species for the destruction of organic dye. In particular, faster adsorption kinetics rate was achieved due to the apparent porosity of and high surface area of WT-1.

$$WTa_{37}O_{95.87} \xrightarrow{hv} e^{-} + h^{+} \quad (7)$$
$$e^{-} + O_2 \rightarrow O_2^{\bullet} \quad (8)$$
$$e^{-} + O_2 + H_2O \rightarrow H_2O_2 \quad (9)$$
$$e^{-} + H_2O_2 \rightarrow OH^{\bullet} + OH^{-} \quad (10)$$
$$h^{+} + H_2O \rightarrow H^{+} + OH^{\bullet} \quad (11)$$
$$h^{+} + OH^{-} \rightarrow OH^{\bullet} \quad (12)$$

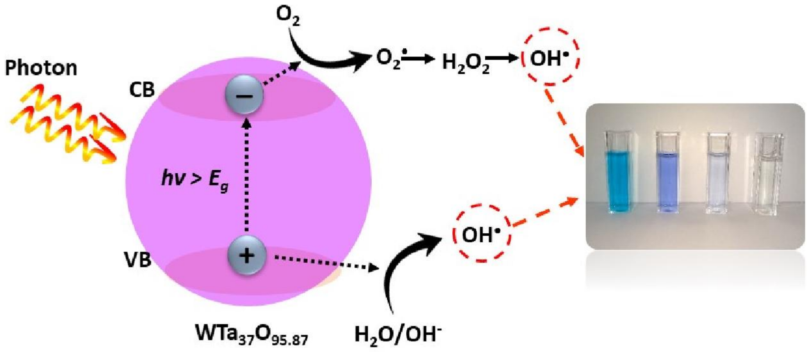

Figure 4. Schematic diagram of photocatalytic degradation of MB by $WTa_{37}O_{95.87}$ nanocatalyst.

3.4. Electronic Properties

In order to report a model and investigate the electronic properties of $WTa_{37}O_{95.487}$, we applied different methods and simulate the bandgap of 2x2x2 supercell of Ta_2O_5 and found that GGA/PBE at PseudoDojo pseudopotential can nicely reproduce the experimental band gap (3.9 eV).[10] Although, the simulated bandgap (3.32 eV, see Figure S6a, and Table S1) of Ta_2O_5 is lower than the experimentally 3.9 eV, the Fermi energy, VB, and CB positions are accurately reproduced.[27] We also simulated a 4.10 eV bandgap for Ta_2O_5 at MGGA at TB09LDA, as given in Figure S6 but the Fermi energy is underestimated so, VB and CB were also at inappropriate positions. Pristine WO_3 has a bandgap of 3.1 eV as reported by Wang's.[39] Using the GGA/PBE at PseudoDojo has also accurately reproduced the bandgap of WO_3. Geometries of Ta_2O_5 unit cell and its supercells are relaxed before simulating their electronic properties. The optimized relaxed structure of the 2x2x2 supercell of Ta_2O_5 along [001] is just used for the interaction study with OH and to predict the catalytic activity. The cohesive formation energy of Ta, W, and O are calculated to validate the method. As reported by Cui et al, we also used the Ta_2O_5(001) model, which has positive surface formation energy.[23]

The PDOS of bulk 4x4x2 supercell of Ta_2O_5 in the range of −10 and +10 eV at Fermi energy of -7.25 eV (vs. vacuum level) is given in Figure 5. The occupied 5d orbitals of Ta are lower in energy than that of the O 2p so, the bonding orbitals of O constitute the valence band while anti-bonding orbitals of Ta (5d) constitute the conduction band. Finally, this results in a bandgap of 2.34 eV. Although, this bandgap is a bit underestimated compared to that of the experiment, the valence band maximum (VBM) and conduction band minimum (CBM) trends are nicely reproduced. From Figures 5a and c, we can see that the upper portion of the valence band (VB) is composed of bonding O 2p states and with a minor contribution of Ta 5d states. The O 2p and Ta 5d states have a good hybridization in the VB state, however, the CB is majorly constituted by the anti-bonding orbitals of Ta 5d, as shown in Figure 5a. The VBM and CBM of pristine 4x4x2 supercell of Ta_2O_5 are listed in Table 2 while that of 2x2x2 supercell of Ta_2O_5 are −7.02 and −4.70 eV (at vacuum), respectively (Table S1).

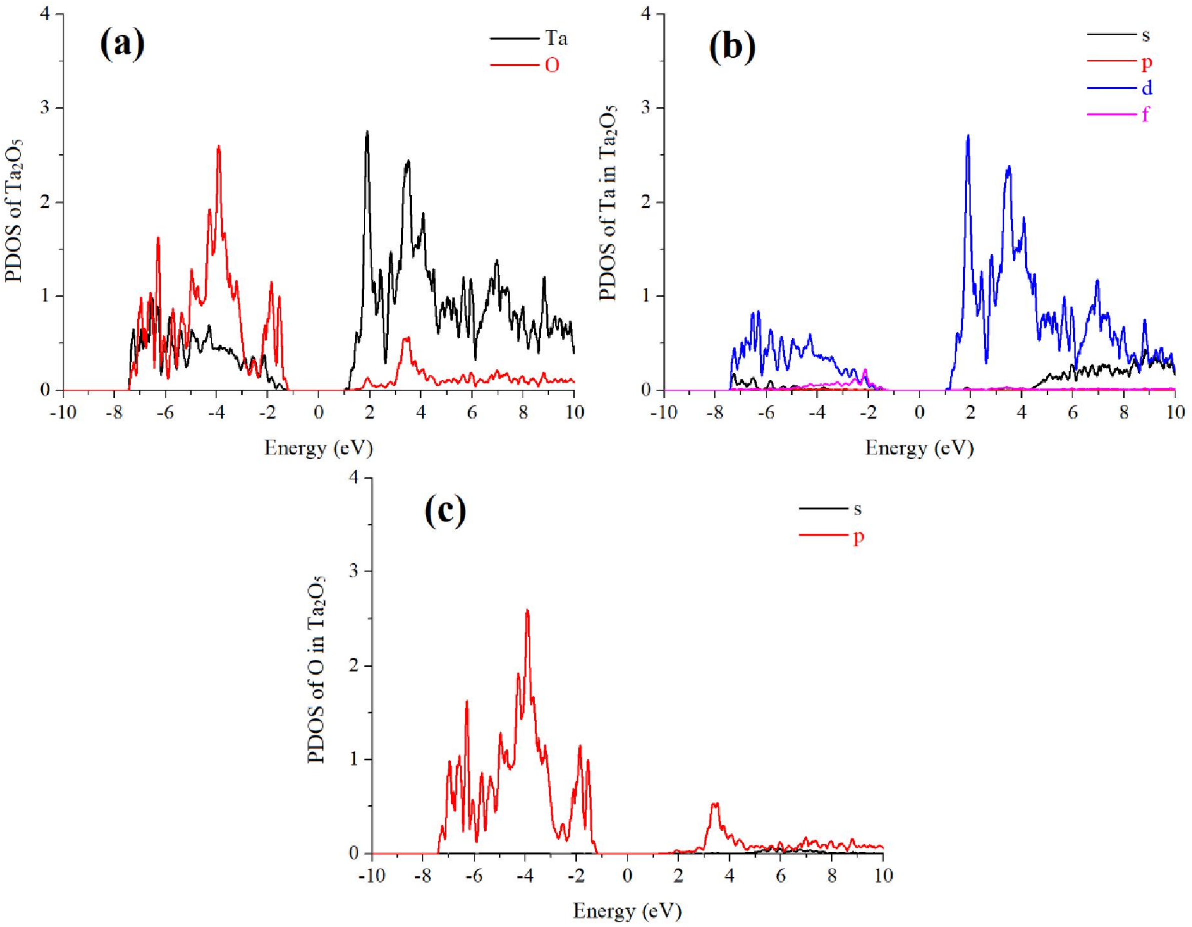

Figure 5. PDOS of 4x4x2 supercell of Ta_2O_5 (a) along with the orbital contribution of Ta (b), and O (c) in a vacuum level. The Fermi energy is set to zero.

Table 2. The Fermi energy, VB, CB, and energy bandgap (eV) of 4x4x2 supercell of Ta_2O_5 and $WTa_{37}O_{95.487}$.

Species	*Fermi Energy*	*VB*	*CB*	*Bandgap (eV)*
Ta_2O_5	-7.25	-1.25	1.09	2.34
$WTa_{37}O_{95.487}$	-6.19	-2.35	-0.05	2.30

In order to correlate the theoretical data with our experiments and propose a novel model, we constructed the $WTa_{37}O_{95.487}$ from Ta_2O_5 (*vide supra*), and the optimized structures are given in Figure S1. As explained earlier, we replaced two of the Ta atoms with W and added one O atom in the 4x4x2 supercell of Ta_2O_5 to represent the $WTa_{37}O_{95.487}$. The electronic properties of the $WTa_{37}O_{95.487}$ nanocatalyst in the form of PDOS along with its individual Ta, W, and O atoms are given in Figure 6 and Table 2. Comparative analysis of the data of Table 2 predicts that Fermi energy and bandgap of 4x4x2 supercell of Ta_2O_5 are decreased to -6.19 and 2.30 eV, from -7.25 and 2.34 eV, respectively. So, it is inferred that the incorporation of W has lowered both the bandgap and Fermi energy of pristine Ta_2O_5. The PDOS of $WTa_{37}O_{95.487}$ in the energy range of −10 and +10 eV is given in Figure 6a. From 6a, we can see that again the VB of $WTa_{37}O_{95.487}$ is majorly composed of bonding orbitals of O 2p along with a minor contribution of W as can be seen from Figure 6a. In addition, the successful incorporation of W in 4x4x2 supercell of Ta_2O_5 can also be predicted from the strong hybridization of both bonding anti-orbitals (5d) of W and Ta atoms as can be seen from Figure 6a-c. While the PDOS of O atoms in $WTa_{37}O_{95.487}$ is similar to that of the pristine 4x4x2 supercell of Ta_2O_5 as shown in Figure 6c. We have seen that occupied 2p orbitals of O constitute the VBM while unoccupied 5d orbitals of Ta constitute the VBM in the 4x4x2 supercell of Ta_2O_5 (see Figure 5). However, in the case of $WTa_{37}O_{95.487}$, the VBM is made of 2p bonding orbitals of O but the CBM is majorly constituted by the anti-bonding orbitals of W (5d), instead of Ta (5d). Besides, W atoms produce an extra band within the bandgap of $WTa_{37}O_{95.487}$, which is closer to the VB. Again, we can say that the reduction in the bandgap of $WTa_{37}O_{95.487}$ is because the W atom, produced extra bands within the bandgap that has reduced its Fermi energy as well. This lower bandgap (2.30 eV) and appropriate positions of the VBM and CBM are ideal for the efficient photocatalytic reaction of $WTa_{37}O_{95.487}$ nanocatalyst. This statement can nicely support our experimentally observed data.

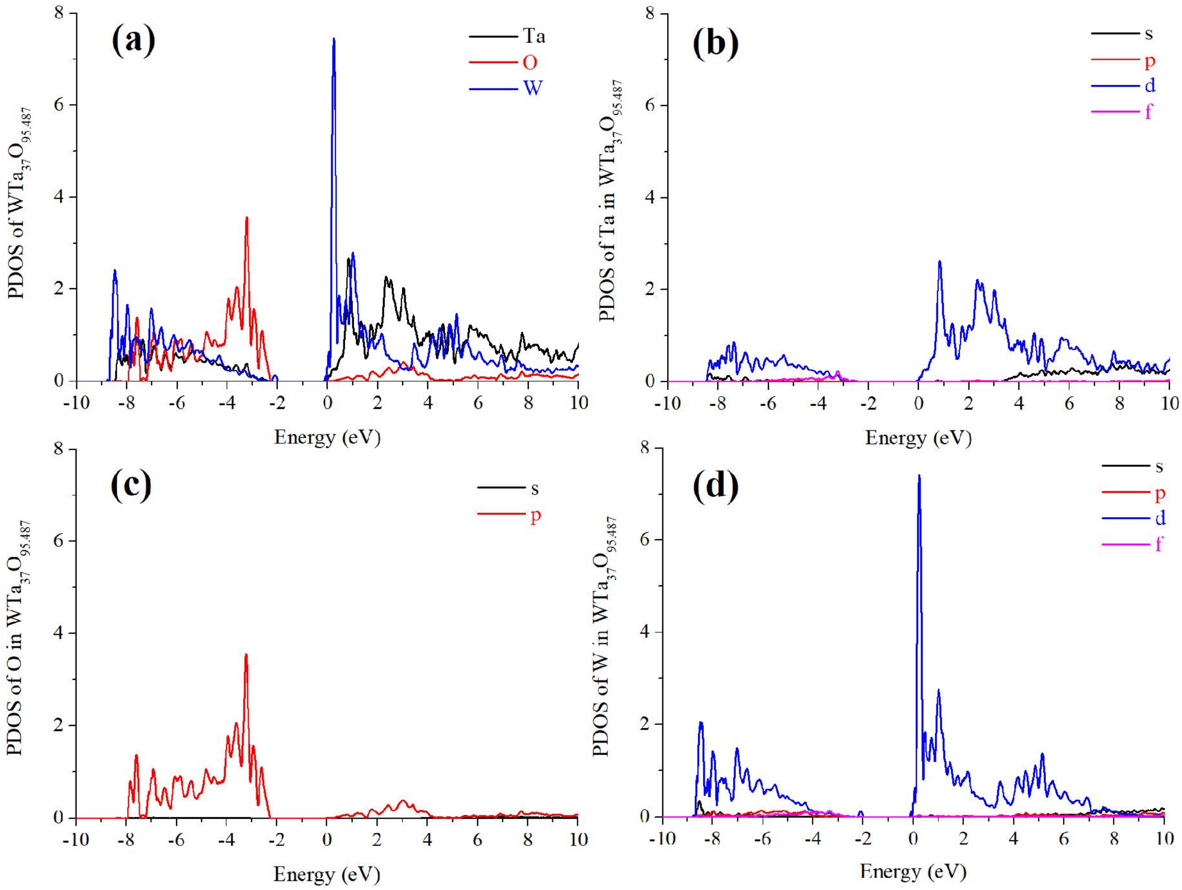

Figure 6. PDOS of (a) $WTa_{37}O_{95.487}$ and its constituents such as (b) Ta, (c) W, and (d) O at vacuum level. The Fermi energy is set to zero.

The band structures of bulk 4x4x2 supercell of Ta_2O_5 and $WTa_{37}O_{95.487}$ are shown in Figure 7, where VBM and CBM are depicted as blue and red lines. Comparative analysis of Figure 7 led us to predict that $WTa_{37}O_{95.487}$ has a narrower bandgap (2.30 eV) than that of the 4x4x2 supercell of Ta_2O_5 (2.34 eV). From Figure 7b, we can see an extra band above the VBM of $WTa_{37}O_{95.487}$, responsible for narrowing the bandgap of Ta_2O_5. A similar trend is observed in the 2x2x2 supercell cell of Ta_2O_5 and its W-doped species as shown in Figure S7 and Table S1 of the Supporting Information.

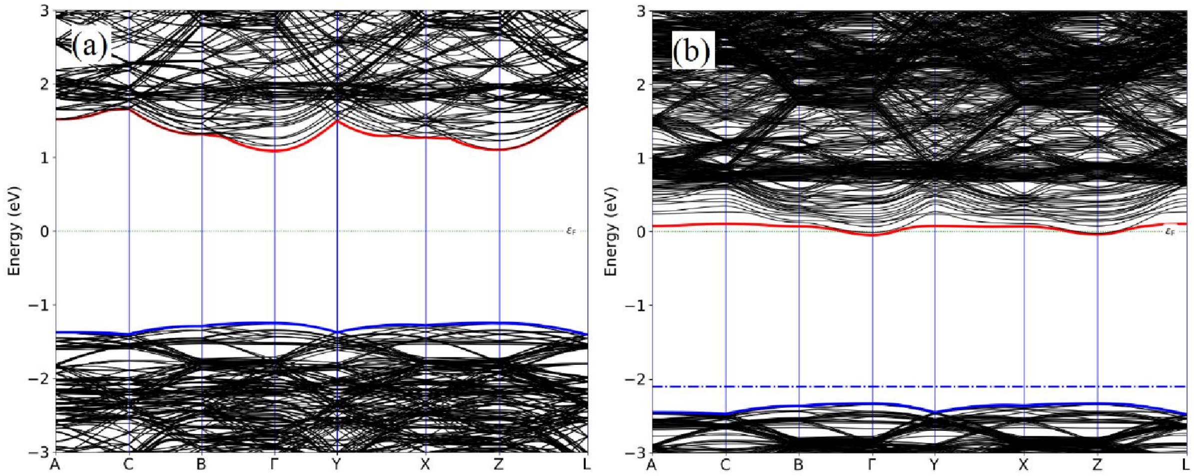

Figure 7. Band structure of 4x4x2 supercell of Ta_2O_5 (a) and $WTa_{37}O_{95.487}$ (b). The Fermi energy was set to zero.

Since the bandgap of both 4x4x2 supercells of Ta_2O_5 and $WTa_{37}O_{95.487}$ are simulated from band structure, we also investigated their optical properties. The optical absorption spectra of 4x4x2 supercell of Ta_2O_5 and $WTa_{37}O_{95.487}$ are simulated along the X, Y, and Z directions as shown in Figure 8, while that of 2x2x2 supercell cell of Ta_2O_5 and its W-doped species are given in Figure S8 of the Supporting Information. As discussed earlier, W atoms produce an extra flat band within the bandgap of $WTa_{37}O_{95.487}$ which consequently reduces its bandgap compared to that of pristine 4x4x2 supercell of Ta_2O_5. From the optical absorption spectral analysis, it can be inferred that the pristine 4x4x2 supercell of Ta_2O_5 has a maximum absorption band peak within the range of 2.0 to 3.5 eV along with a minor absorption band peak at around 0.1 eV (Figure 8a). On the other hand, the maximum absorption band peak of $WTa_{37}O_{95.487}$ is in the range of 0 to 1.0 eV along with another absorption band peak of ~ 2.0 to 3.0 eV. So, again as observed in the band structure and PDOS analyses, a similar trend is found in the optical absorption spectra of 4x4x2 supercell of Ta_2O_5 and $WTa_{37}O_{95.487}$. We can say, that the maximum absorption band peak in 0 to 1 eV of $WTa_{37}O_{95.487}$ is due to the merging of Fermi level within its CBM.

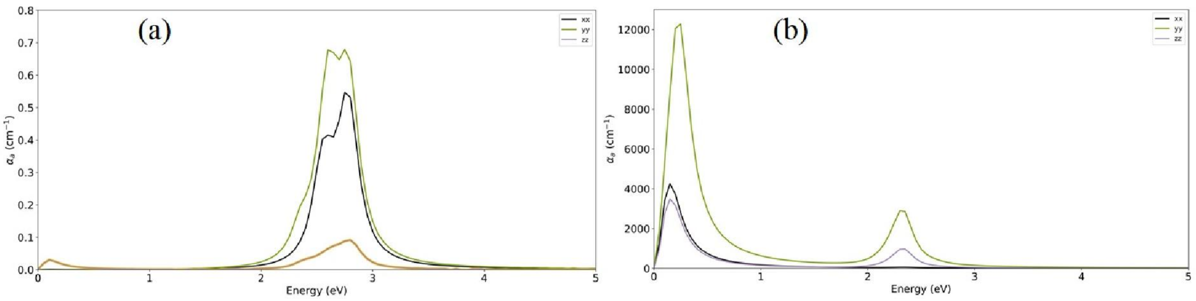

Figure 8: Optical absorption spectra of 4x4x2 supercell of Ta_2O_5 (a) and $WTa_{37}O_{95.487}$ (b).

Furthermore, the catalytic activity of these two species is predicted from the interaction of the OH group. For this study, we used the 2x2x2 supercell of Ta_2O_5 along [001] direction and its W-doped species. The adsorption of hydroxyl is non-dissociative where the O of OH group interacts with the Ta and W of 2x2x2Ta_2O_5(001) and W-doped 2x2x2Ta_2O_5(001), respectively, as shown in Figure 9. The adsorption energy of this non-covalent bonding in 2x2x2Ta_2O_5(001)@OH is about -11.76 kcal mol^{-1} while -19.83 kcal mol^{-1} in the case of the W-doped 2x2x2Ta_2O_5(001)@OH system (see Figure 9). This stronger interaction in the W-doped 2x2x2Ta_2O_5(001)@OH system predicts the excellent catalytic of the $WTa_{37}O_{95.487}$ system compared to pristine Ta_2O_5 (*vide supra*). The adsorption energy of the OH group over the surfaces of 2x2x2Ta_2O_5(001) and W-doped 2x2x2Ta_2O_5(001) was calculated from the difference in energies of the optimized OH group and adsorbent (E_{slab}) from the optimized OH-slab complex (*slab@OH*), using equation (13).

$$\Delta E_{ad} = E_{slab@OH} - (E_{OH} + E_{slab}) \quad (13)$$

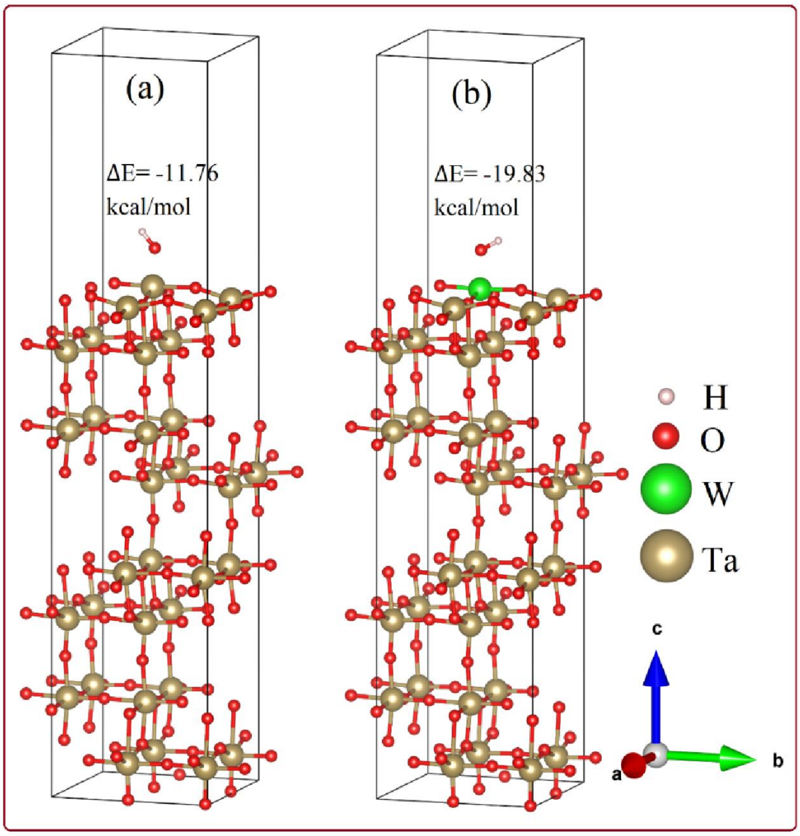

Figure 9. Optimized structures of (a) 2x2x2Ta_2O_5(001)@OH and (b) W-doped 2x2x2Ta_2O_5(001)@OH.

Finally, the charge distribution analysis of 2x2x2Ta_2O_5(001), W-doped 2x2x2Ta_2O_5(001), and their OH interactive systems are simulated from the electron density difference (EDD). The 2D EDD plots and their respective electrostatic potential plots are shown in Figure 10. Besides, the comparative EDD plots of 2x2x2Ta_2O_5(001) and W-doped 2x2x2Ta_2O_5(001) are shown in Figure S9, where we can see the successful incorporation of the W atom. In addition, this sharing of charge produces a strong hybridization between the orbitals of Ta and W atoms which finally improves the catalytic activity (*vide supra*) and stability. The blue and green shaded areas of Figure 10 denote charge accumulation and depletion, respectively. Comprehensive analysis of these EDD plots led us to predict that a significant amount of electronic cloud density is shared between OH and W-doped 2x2x2Ta_2O_5(001) in the W-doped

2x2x2Ta_2O_5(001)@OH system. This charge transferring is higher than that of the 2x2x2Ta_2O_5(001)@OH system.

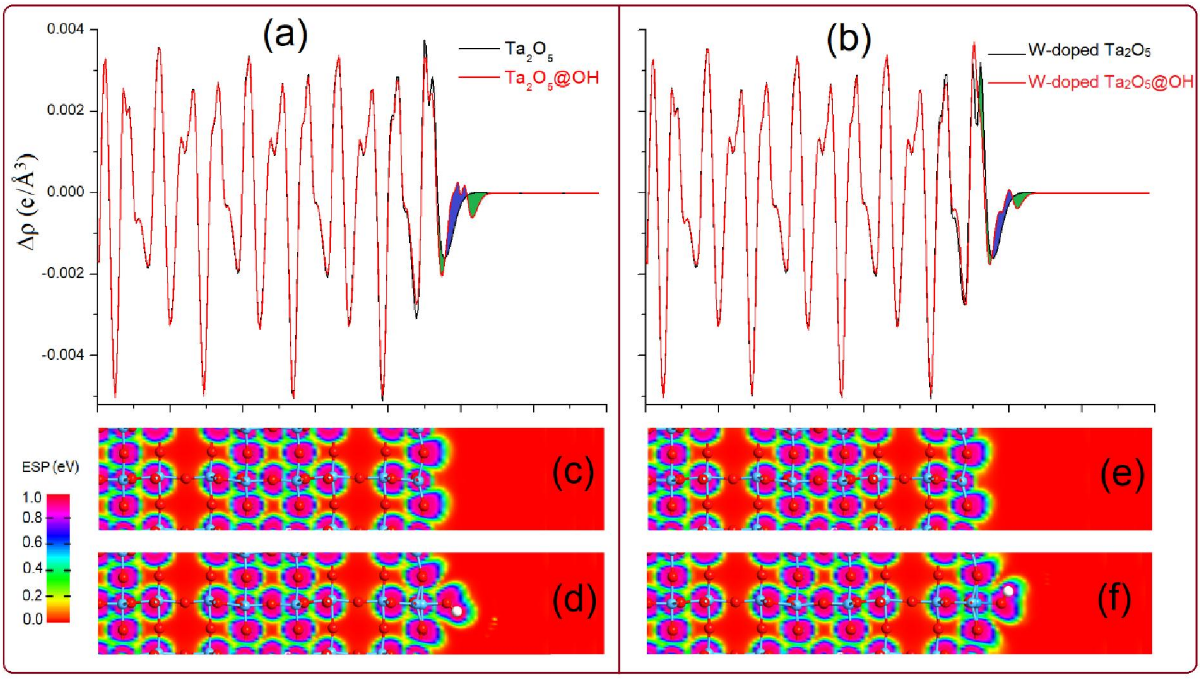

Figure 10. The electron density difference (*Δρ*) in the Z-direction for 2x2x2Ta_2O_5(001) and its OH interacted system (a) W-doped 2x2x2Ta_2O_5(001) and its OH interacted system (b). The blue and green shaded areas show electron accumulation and donation, respectively. Electrostatic potential map (ESP) of 2x2x2Ta_2O_5(001) (c), W-doped 2x2x2Ta_2O_5(001)@OH (d), W-doped 2x2x2Ta_2O_5(001) (e) and W-doped 2x2x2Ta_2O_5(001)@OH systems (f).

In summary, we found that either model of $WTa_{37}O_{95.487}$ produce similar trends and corroborate the experimental data. However, we suggest that further deep investigation of $WTa_{37}O_{95.487}$ is crucial as this material has not been properly studied since 1971. Besides, we recommend that our proposed model can be used as a landmark for future researchers. Again, we can say that $WTa_{37}O_{95.487}$ has excellent performance compared to that of pristine Ta_2O_5. The possible explanation for this might be the proper amount of W atoms in $WTa_{37}O_{95.487}$ nanocatalyst, which is responsible for higher catalytic activity. Thus, the addition of the W atom can improve the overall performance of $WTa_{37}O_{95.487}$, and does not distort the parental geometry of Ta_2O_5.

4. Conclusion

In this work, we report a wide bandgap $WTa_{37}O_{95.487}$ photocatalyst, using density functional theory (DFT) and an experimental approach. This material ($WTa_{37}O_{95.487}$) was reported for the first time by N. Stephenson *et al.* in 1971[16], but no one has investigated its photocatalytic properties. The reason behind this is its wide bandgap and complicated crystal structure. Herein, we have designed and reported two different types of models for the DFT investigation which are followed by a simple and low-cost co-precipitation synthetic method. The $WTa_{37}O_{95.487}$ prepared at 150 °C (WT-1) demonstrates efficient photocatalytic activity for methylene blue decolorization due to surface dispersibility and porosity. The degradation efficiency and pseudo kinetic constant, k_{app} of WT-1 attained 99 % and 0.0321 min^{-1}, respectively within 60 min under 100 $mWcm^{-2}$ simulated sunlight. The degradation efficiency achieved almost 100 % within 30 min with $k_{app} = 0.0643$ min^{-1} under 200 $mWcm^{-2}$ for the same nanocatalyst powder which infers that the kinetics of the photocatalytic process is proportionally dependent on an increase in light intensity. Finally, a good correlation of theoretical and experimental results validates and confirms the efficient catalytic performance of our proposed nanocatalyst.

ASSOCIATED CONTENT

Supporting Information

The crystal structure of Ta_2O_5, $WTa_{37}O_{95.487}$, 2x2x2 supercell of Ta_2O_5 and W-doped 2x2x2 supercell of Ta_2O_5, average particle size, BET surface area, calculation of quantum yield (Φ), turnover number (TON) and turnover frequency (TOF), simulated band gap, Fermi energy, band structure, optical absorption spectra and average electron density for W-doped 2x2x2 supercell of Ta_2O_5(001) and 2x2x2 supercell of Ta_2O_5, are provided in the Supporting Information.

AUTHOR INFORMATION

Corresponding Authors

Siti Nur Farhana Mohd Nasir − Solar Energy Research Institute (SERI), National University of Malaysia, 43600 Bangi, Selangor, Malaysia.; Department of Community Health, Faculty of Medicine, Universiti Kebangsaan Malaysia, 56000 Cheras, Kuala Lumpur, Malaysia orcid.; Email: farhanaana98@gmail.com

Habib Ullah − Environment and Sustainability Institute (ESI), University of Exeter, Penryn Campus, Penryn, Cornwall TR10 9FE, UK; orcid.org/0000-0001-9290-0265; Email: hu203@exeter.ac.uk

Mohd Asri Mat Teridi − Solar Energy Research Institute (SERI), National University of Malaysia, 43600 Bangi, Selangor, Malaysia.; orcid.org/0000-0003-2812-8447; Email: asri@ukm.edu.my

Authors

Muhazri Abd Mutalib − Solar Energy Research Institute (SERI), National University of Malaysia, 43600 Bangi, Selangor, Malaysia.

Farah Husna Saifuddin − Solar Energy Research Institute (SERI), National University of Malaysia, 43600 Bangi, Selangor, Malaysia.

Nurul Affiqah Arzaee − Solar Energy Research Institute (SERI), National University of Malaysia, 43600 Bangi, Selangor, Malaysia.

Asif Ali Tahir − Environment and Sustainability Institute (ESI), University of Exeter, Penryn Campus, Penryn, Cornwall TR10 9FE, UK

Mohamad Firdaus Mohamad Noh − Solar Energy Research Institute (SERI), National University of Malaysia, 43600 Bangi, Selangor, Malaysia.

Mohd Adib Ibrahim − Solar Energy Research Institute (SERI), National University of Malaysia, 43600 Bangi, Selangor, Malaysia.

Hazim Moria − Department of Mechanical Engineering Technology, Yanbu Industrial College, PO Box 30436, 41912 Yanbu Alsinaiyah, Saudi Arabia.

Mohammed N. Alghamdi − Department of Mechanical Engineering Technology, Yanbu Industrial College, PO Box 30436, 41912 Yanbu Alsinaiyah, Saudi Arabia.

Author Contributions

The manuscript was written through the contributions of all authors. All authors have given approval to the final version of the manuscript.

Notes

The authors declare no competing financial interest.

ACKNOWLEDGMENTS

The authors would like to acknowledge financial support from the National University of Malaysia and the Center for Research and Instrumentation (CRIM) through internal grants MI-2019-004, DIP-2015-005, and also for providing facilities to perform this research. HU and AAT are thankful to the Engineering and Physical Science Research Council, UK (EPSRC under the research grant no. EP/V049046/1 and EP/T025875/1) for financial support. SNFM would like to thank to Associate Professor Dr. Ahed Husni A. Zyoud (An-Najah National University) for insightful discussion.

Data availability

The data that support the findings of this study are available from the corresponding author upon reasonable request.

REFERENCE

(1) Rafatullah, M.; Sulaiman, O.; Hashim, R.; Ahmad, A. Adsorption of Methylene Blue on Low-Cost Adsorbents: A Review. *J. Hazard. Mater.* **2010**, *177* (1), 70–80.

(2) Ponnusami, V.; Madhuram, R.; Krithika, V.; Srivastava, S. N. Effects of Process Variables on Kinetics of Methylene Blue Sorption onto Untreated Guava (Psidium Guajava) Leaf Powder: Statistical Analysis. *Chem. Eng. J.* **2008**, *140* (1), 609–613.

(3) Shirmardi, A.; Teridi, M. A. M.; Azimi, H. R.; Basirun, W. J.; Jamali-Sheini, F.; Yousefi, R. Enhanced Photocatalytic Performance of ZnSe/PANI Nanocomposites for Degradation of Organic and Inorganic Pollutants. *Appl. Surf. Sci.* **2018**, *462*, 730–738.

(4) Ghoreishi, K. B.; Asim, N.; Che Ramli, Z. A.; Emdadi, Z.; Yarmo, M. A. Highly Efficient Photocatalytic Degradation of Methylene Blue Using Carbonaceous WO_3/TiO_2 Composites. *J. Porous Mater.* **2016**, *23* (3), 629–637.

(5) Che Ramli, Z. A.; Asim, N.; Isahak, W. N. R. W.; Emdadi, Z.; Ahmad-Ludin, N.; Yarmo, M. A.; Sopian, K. Photocatalytic Degradation of Methylene Blue under UV Light Irradiation on Prepared Carbonaceous TiO_2. *Sci. World J.* **2014**, *2014*, 415136.

(6) Pudukudy, M.; Yaakob, Z.; Rajendran, R.; Kandaramath, T. Photodegradation of Methylene Blue over Novel 3D ZnO Microflowers with Hexagonal Pyramid-like Petals. *React. Kinet. Mech. Catal.* **2014**, *112* (2), 527–542.

(7) Ahmed, Y.; Yaakob, Z.; Akhtar, P. Degradation and Mineralization of Methylene Blue Using a Heterogeneous Photo-Fenton Catalyst under Visible and Solar Light Irradiation. *Catal. Sci. Technol.* **2016**, *6* (4), 1222–1232.

(8) Peik-See, T.; Pandikumar, A.; Ngee, L. H.; Ming, H. N.; Hua, C. C. Magnetically

Separable Reduced Graphene Oxide/Iron Oxide Nanocomposite Materials for Environmental Remediation. *Catal. Sci. Technol.* **2014**, *4* (12), 4396–4405.

(9) Liu, X.; Pan, L.; Chen, T.; Li, J.; Yu, K.; Sun, Z.; Sun, C. Visible Light Photocatalytic Degradation of Methylene Blue by SnO_2 Quantum Dots Prepared via Microwave-Assisted Method. *Catal. Sci. Technol.* **2013**, *3* (7), 1805–1809.

(10) Kato, H.; Kudo, A. New Tantalate Photocatalysts for Water Decomposition into H_2 and O_2. *Chem. Phys. Lett.* **1998**, *295* (5), 487–492.

(11) Krishnaprasanth, A.; Seetha, M. Solvent Free Synthesis of Ta_2O_5 Nanoparticles and Their Photocatalytic Properties. *AIP Adv.* **2018**, *8* (5), 55017.

(12) Parida, K. M.; Mahanta, S. K.; Martha, S.; Nashim, A. Fabrication of NiO/Ta_2O_5 Composite Photocatalyst for Hydrogen Production under Visible Light. *Int. J. Energy Res.* **2013**, *37* (2), 161–170.

(13) Xu, L.; Guan, J.; Shi, W. Enhanced Interfacial Charge Transfer and Visible Photocatalytic Activity for Hydrogen Evolution from a Ta_2O_5-Based Mesoporous Composite by the Incorporation of Quantum-Sized CdS. *ChemCatChem* **2012**, *4* (9), 1353–1359.

(14) Xu, L.; Guan, J.; Shi, W.; Liu, L. Heterostructured Mesoporous In_2O_3/Ta_2O_5 Composite Photocatalysts for Hydrogen Evolution: Impacts of In_2O_3 Content and Calcination Temperature. *J. Colloid Interface Sci.* **2012**, *377* (1), 160–168.

(15) Stephenson, N. C.; Roth, R. S. Structural Systematics in the Binary System Ta_2O_5–WO_3. V. The Structure of the Low-Temperature Form of Tantalum Oxide L-Ta_2O_5. *Acta Crystallogr. Sect. B* **1971**, *27* (5), 1037–1044.

(16) Stephenson, N. C.; Roth, R. S. Structural Systematics in the Binary System Ta_2O_5–WO_3. IV. The Structure of $Ta_{38}WO_{98}$. *Acta Crystallogr. Sect. B* **1971**, *27* (5), 1031–1036.

(17) Chorney, M. Investigations of Solid-State Sintering Behavior of Binary Refractory Metal Oxide Systems. Thesis. **2018**.

(18) Mutalib, M. A.; Aziz, F.; Jamaludin, N. A.; Yahya, N.; Ismail, A. F.; Mohamed, M. A.; Yusop, M. Z. M.; Salleh, W. N. W.; Jaafar, J.; Yusof, N. Enhancement in Photocatalytic Degradation of Methylene Blue by $LaFeO_3$-GO Integrated Photocatalyst-Adsorbents under Visible Light Irradiation. *Korean J. Chem. Eng.* **2018**, *35* (2), 548–556.

(19) Mohamed, M. A.; W. Salleh, W. N.; Jaafar, J.; Ismail, A. F.; Mutalib, M. A.; Sani, N. A. A.; M. Asri, S. E. A.; Ong, C. S. Physicochemical Characteristic of Regenerated Cellulose/N-Doped TiO_2 Nanocomposite Membrane Fabricated from Recycled Newspaper with Photocatalytic Activity under UV and Visible Light Irradiation. *Chem. Eng. J.* **2016**, *284*, 202–215.

(20) Choudhry, G.G. and Webster, G. R. Environmental Photochemistry of PCDDs. Part I. Kinetic and Quantum Yields of the Photodegradation of 1,2,3,4,7-Penta-and 1,2,3,4,7,8-Hexachlorodiabenzo-PDioxin in Aqueous Acetonitrile. *Chemosphere* **1985**, *14* (1), 9–26.

(21) Gomathi Devi, L.; Shyamala, R. Photocatalytic Activity of SnO2–α-Fe2O3 Composite Mixtures: Exploration of Number of Active Sites, Turnover Number and Turnover Frequency. *Mater. Chem. Front.* **2018**, *2* (4), 796–806.

(22) Søren Smidstrup, Troels Markussen, Pieter Vancraeyveld, Jess Wellendorff, Julian Schneider, Tue Gunst, Brecht Verstichel, Daniele Stradi, Petr A. Khomyakov, Ulrik G. Vej-Hansen, Maeng-Eun Lee, Samuel T. Chill, Filip Rasmussen, Gabriele Penazzi, Fabiano Co, K. S. QuantumATK: An Integrated Platform of Electronic and Atomic-Scale Modelling Tools. *J. Phys. Condens. Matter* **2020**, *32*, 015901.

(23) Cui, Z.-H.; Jiang, H. Theoretical Investigation of Ta_2O_5, TaON, and Ta_3N_5: Electronic Band Structures and Absolute Band Edges. *J. Phys. Chem. C* **2017**, *121* (6), 3241–3251.

(24) Enkovaara, J.; Rostgaard, C.; Mortensen, J. J.; Chen, J.; Dułak, M.; Ferrighi, L.; Gavnholt, J.; Glinsvad, C.; Haikola, V.; Hansen, H. A.; et al. Electronic Structure Calculations with GPAW: A Real-Space Implementation of the Projector Augmented-Wave Method. *J.*

Phys. Condens. Matter **2010**, *22* (25), 253202.

(25) Van Setten, M. J.; Giantomassi, M.; Bousquet, E.; Verstraete, M. J.; Hamann, D. R.; Gonze, X.; Rignanese, G.-M. The PseudoDojo: Training and Grading a 85 Element Optimized Norm-Conserving Pseudopotential Table. *Comput. Phys. Commun.* **2018**, *226*, 39–54.

(26) Kresse, G.; Joubert, D. From Ultrasoft Pseudopotentials to the Projector Augmented-Wave Method. *Phys. Rev. B* **1999**, *59* (3), 1758–1775.

(27) Chun, W.-J.; Ishikawa, A.; Fujisawa, H.; Takata, T.; Kondo, J. N.; Hara, M.; Kawai, M.; Matsumoto, Y.; Domen, K. Conduction and Valence Band Positions of Ta_2O_5, TaON, and Ta_3N_5 by UPS and Electrochemical Methods. *J. Phys. Chem. B* **2003**, *107* (8), 1798–1803.

(28) Nandiyanto, A. B. D.; Zaen, R.; Oktiani, R. Correlation between Crystallite Size and Photocatalytic Performance of Micrometer-Sized Monoclinic WO_3 Particles. *Arab. J. Chem.* **2020**, *13* (1), 1283–1296.

(29) Ohtani, B.; Ogawa, Y.; Nishimoto, S. Photocatalytic Activity of Amorphous−Anatase Mixture of Titanium(IV) Oxide Particles Suspended in Aqueous Solutions. *J. Phys. Chem. B* **1997**, *101* (19), 3746–3752.

(30) Sharma, J.; Vashishtha, M.; Shah,; D. O. Crystallite Size Dependence on Structural Parameters and Photocatalytic Activity of Microemulsion Mediated Synthesized ZnO Nanoparticles Annealed at Different Temperatures. *Glob. J. Sci. Front. Res* **2014**, *14*, 19–32.

(31) Houas, A.; Lachheb, H.; Ksibi, M.; Elaloui, E.; Guillard, C.; Herrmann, J.-M. Photocatalytic Degradation Pathway of Methylene Blue in Water. *Appl. Catal. B Environ.* **2001**, *31* (2), 145–157.

(32) Shahwan, T.; Abu Sirriah, S.; Nairat, M.; Boyacı, E.; Eroğlu, A. E.; Scott, T. B.; Hallam, K. R. Green Synthesis of Iron Nanoparticles and Their Application as a Fenton-like Catalyst for the Degradation of Aqueous Cationic and Anionic Dyes. *Chem. Eng. J.* **2011**, *172* (1), 258–266.

(33) Rauf, M. A.; Meetani, M. A.; Khaleel, A.; Ahmed, A. Photocatalytic Degradation of Methylene Blue Using a Mixed Catalyst and Product Analysis by LC/MS. *Chem. Eng. J.* **2010**, *157* (2), 373–378.

(34) Zhang, T.; Oyama, T.; Aoshima, A.; Hidaka, H.; Zhao, J.; Serpone, N. Photooxidative N-Demethylation of Methylene Blue in Aqueous TiO_2 Dispersions under UV Irradiation. *J. Photochem. Photobiol. A Chem.* **2001**, *140* (2), 163–172.

(35) Zyoud, A.; Zu'bi, A.; Helal, M. H. S.; Park, D.; Campet, G.; Hilal, H. S. Optimizing Photo-Mineralization of Aqueous Methyl Orange by Nano-ZnO Catalyst under Simulated Natural Conditions. *J. Environ. Heal. Sci. Eng.* **2015**, *13* (1), 46.

(36) Zyoud, A. H.; Zorba, T.; Helal, M.; Zyoud, S.; Qamhiya, N.; Hajamohideen, A.-R.; Zyoud, S.; Hilal, H. S. Direct Sunlight-Driven Degradation of 2-Chlorophenol Catalyzed by Kaolinite-Supported ZnO. *Int. J. Environ. Sci. Technol.* **2019**, *16* (10), 6267–6276.

(37) Reza, K. M.; Kurny, A. S. W.; Gulshan, F. Parameters Affecting the Photocatalytic Degradation of Dyes Using TiO_2: A Review. *Appl. Water Sci.* **2017**, *7* (4), 1569–1578.

(38) Gaya, U. I.; Abdullah, A. H. Heterogeneous Photocatalytic Degradation of Organic Contaminants over Titanium Dioxide: A Review of Fundamentals, Progress and Problems. *J. Photochem. Photobiol. C Photochem. Rev.* **2008**, *9* (1), 1–12.

(39) Wang, F.; Di Valentin, C.; Pacchioni, G. Electronic and Structural Properties of WO_3: A Systematic Hybrid DFT Study. *J. Phys. Chem. C* **2011**, *115* (16), 8345–8353.

TOC Graphic

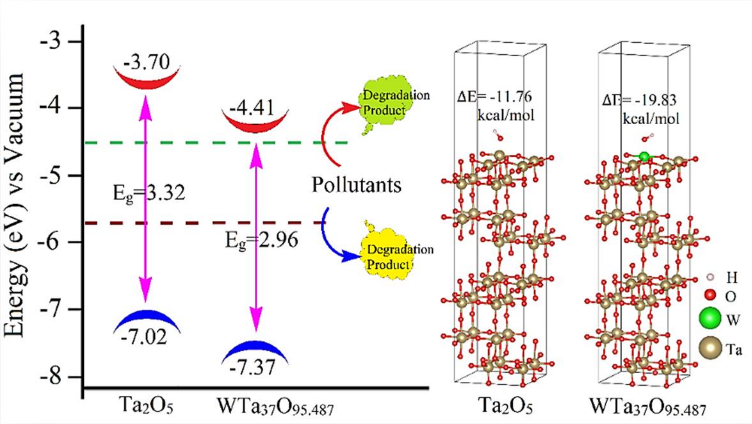
Energy (eV) vs Vacuum
-3
-4
-5
-6
-7
-8
-3.70
-4.41
E_g=3.32
E_g=2.96
-7.02
-7.37
Degradation Product
Pollutants
Degradation Product
Ta_2O_5
$WTa_{37}O_{95.487}$
ΔE= -11.76 kcal/mol
ΔE= -19.83 kcal/mol
H
O
W
Ta
Ta_2O_5
$WTa_{37}O_{95.487}$